# Nanoscale

Accepted Manuscript


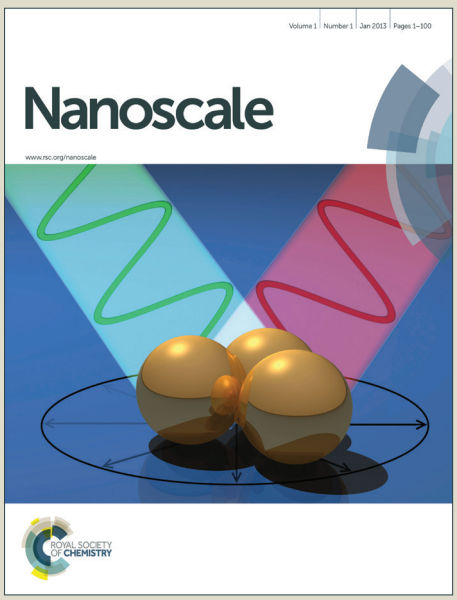





ROYAL SOCIETY OF CHEMISTRY

www.rsc.org/nanoscale

Nanoscale

RSCPublishing

ARTICLE

# Conversion of Silica Nanoparticles into Si Nanocrystals through Electrochemical Reduction

Cite this: DOI: 10.1039/x0xx00000x

Hirotomo Nishihara,*[a] Takashi Suzuki,[a] Hiroyuki Itoi,[ab] Bai-Gang An,[ac] Shinichiroh Iwamura,[ad] Raúl Ber-enguer[ae] and Takashi Kyotani[a]

Received 00th January 2012,
Accepted 00th January 2012

DOI: 10.1039/x0xx00000x

www.rsc.org/

The precise design at nanometer scale of Si-based materials is a quite complex issue but of utmost importance for their present and potential applications. This paper reports the first attempt to address the electrochemical reduction of $SiO_2$ at nanometer scale. $SiO_2$ nanoparticles are first covered with a uniform carbon layer with controlled thickness at an accuracy of a few nanometers, by pressure-pulsed chemical vapor deposition. With appropriate thickness, the carbon layer plays significant roles as a current path and also as a physical barrier against Si-crystal growth, and the $SiO_2$ nanoparticles are successfully converted into extremely small Si nanocrystals (< 20 nm) inside the shell-like carbon layer whose morphology is derived from the original $SiO_2$ nanoparticles. Thus, the proposed electroreduction method offers a new synthesis strategy of Si/C nanocomposites utilizing the morphology of $SiO_2$ nanomaterials, which are well known for wide variety of defined and regular nanostructures. Owing to the volume difference of $SiO_2$ and the corresponding Si, nanopores are generated around the Si nanocrystals. It has been demonstrated that the nanopores around the Si nanocrystals are effective to improve cycle performance of Si as a negative electrode for lithium-ion batteries. The present method is in principle applicable to various $SiO_2$ nanomaterials, and thus, offers production of a variety of Si/C composites whose carbon nanostructures can be defined by their parent $SiO_2$ nanomaterials.

## 1. Introduction

Silicon (Si) is the second most abundant element in the earth's crust and is environmentally harmless. Furthermore, it is one of the most important semiconductor materials, so that it has been widely used for electronics and solar cells.[1,2,3,4] When its size is decreased down to nanometer-level, unique quantum properties appear, and such nano-sized Si (nano-Si) is expected to be used for many applications, e.g., electroluminescence, 3-dimensional optical waveguide, and optical cavity.[5,6,7,8,9,10] Si, especially nano-Si, is also known as one of the most promising negative-electrode materials for next-generation lithium-ion batteries (LIBs),[11,12,13,14,15,16,17] owing to its very large capacity (ca. 3578 mAh $g^{-1}$ as $Li_{3.75}Si$) and relatively low lithiation/delithiation potential (0.2~0.5 V vs. $Li/Li^+$). In many of the applications mentioned above, the structure, dimensions, and/or morphology play a key role in the performance of Si. So far, a variety of methods have been proposed to produce Si materials with unique nano- or microstructures, such as anodic etching for quantum porous Si,[8,18,19] solution process,[17,20,21,22] a method combining laser ablation cluster formation and vapor-liquid-solid growth for Si nanowires,[23] and chemical vapor deposition (CVD) for Si nanoparticles and nanowires.[24,25] For the purpose of LIB anodes, the combination with carbon is also of practical importance because it improves the electric conductivity, and the precise structure-control of not only Si but also carbon is a key factor to achieve high performance.[26,27] Si/carbon (Si/C) nanocomposite materials have been prepared based on the Si nanomaterials without much attention to the control of carbon structure, for example just by the mixing with nanocarbons,[17,28] or by the carbon-coating of Si nanomaterials.[16,29,30] It is also common to produce Si/C nanocomposites by depositing Si nanoparticles/nanolayers on nanostructured carbon materials.[14,31] On the other hand, new synthesis techniques for Si/C composites, such as template-assisted synthesis,[32,33] have been developed recently, and such new techniques allow the control of carbon nanostructure, thereby expanding the variety and controllability of Si/C nanostructure.

The control of Si structure, especially at a nanometer-level, is still a challenging target, but it is well known that $SiO_2$ can be easily molded into various forms, with a high precision at nano/microscale, e.g., nanoparticles, nanofibers, nanotubes, multiple mesoporous silicas, ordered mesoporous membrane, macroporous monoliths, opals, inverse opals, and biosilicas having unique and beautiful structures.[34,35,36,37,38,39,40,41,42,43] Therefore, it is reasonably expected that the synthesis of nano-Si from nano-$SiO_2$ would greatly progress the controllability of Si nanostructure.

There are several methods to convert $SiO_2$ into Si. Industrially, high-purity silica is reacted with carbonaceous matters, such as charcoal and coal, at a very high temperature (>2173 K) according to the following equation:

$$SiO_2 + 2C \rightarrow Si + 2CO \quad (1)$$

Since Si is obtained through a liquid phase (m.p. of Si is 1687 K) in this case, it is impossible to obtain nano-Si. Thus, for the conversion of nano-$SiO_2$ into nano-Si, it would be necessary to use a method that works at much lower temperatures, such as a chemical reduction using Mg gas at 923 K[44] or an electrochemical reduction of $SiO_2$ in molten salts below 1123 K.[45,46,47,48,49,50] Considering less significant side reaction and better controllability of the reaction, we have selected the latter method to convert nano-$SiO_2$ into nano-Si based on the following equation:

$$SiO_2 + 4e^- \rightarrow Si + 2O^{2-} \quad (2)$$

The electrochemical reduction of $SiO_2$ into Si has been originally developed by Nohira *et al.*,[45] and so far this method has been applied to bulky $SiO_2$, such as glass-plates, or pellets composed of sintered powder.[45,51,52] The reaction (2) takes place at the three-phase interface of a reactant ($SiO_2$), a conductive path (Si or current corrector), and a reservoir of $O^{2-}$ (molten salts).[45] Consequently, the reaction starts from the outside surface of the bulk $SiO_2$ that keeps in contact with a current collector and a molten salt, and then proceeds to the depth direction alongside the growing conductive Si. Since the propagation of the three-phase interface requires of electric contact with the external current collector, the electroreduction of $SiO_2$ materials necessarily gives rise to interconnected and/or aggregated fibrous Si crystals with a diameter of several micron-meters. In this work, we report for the first time the electrochemical reduction of $SiO_2$ nanoparticles into Si nanocrystals. For the purpose of the direct conversion of nano-$SiO_2$ into nano-Si, the nano-$SiO_2$ precursor was covered with a carbon nanolayer (Fig. 1a) before the electrochemical reduction. The carbon layer replicates the original morphology of the $SiO_2$ nanomaterials, but contains some defects and/or small holes through which molten $CaCl_2$ can get into the inside during the electrochemical reduction (Fig. 1b). During the reduction, the carbon layer not only serves an electron path to facilitate the reduction process, but also plays a key role of a physical barrier restricting the growth of large Si crystals. Consequently, unique Si/C nanocomposites, consisting of individual Si nanocrystals covered by carbon nanoshells with the morphology of parent $SiO_2$ nanomaterials, can be obtained as shown in Fig. 1c after the removal of unreduced $SiO_2$.

## 2. Experimental section

### 2.1 Preparation of carbon-coated SNP

An aqueous solution containing $SiO_2$ nanoparticle (SNP; Snowtex® O-40, Nissan Chemical Industries, Ltd.) was dried up to obtain fine powder of SNP. Then, the powder (ca. 0.1 g) was molded into a pellet (the diameter is 13 mm and the thickness is 0.6 mm) by loading 590 MPa at room temperature. The porosity of the resulting pellet is ca. 59%. The pellet was then calcined at 1123 K for 3 h to improve its mechanical strength. Almost no shrinkage was observed in the whole pellet shape before and after the calcination. Generally, it is difficult to uniformly cover the surface of $SiO_2$, since is it inactive for carbon deposition below the self-decomposition temperature of carbon sources (hydrocarbons). Therefore, the pellet consisting of SNP was subjected to a pressure-pulsed chemical vapor deposition (P-CVD) where a cycle of evacuation (20 s) followed by acetylene feed (20 vol% in $N_2$, for 1 s) was repeated at 1073 K.[16] By the P-CVD method, it is possible to uniformly coat the entire surface of inactive nanoparticles above the decomposition temperature of carbon sources.[16] Then, the sample was further annealed at 1223 K for 1 h under vacuum to obtain carbon-coated SNP. By changing the number of times of acetylene feed in P-CVD to 150, 300, and 500, the carbon-loading amount in the carbon-coated SNP can be controlled to be 6, 12, and 18 wt%, respectively. These samples are referred to as SNP/C(6), SNP/C(12), and SNP/C(18), respectively.

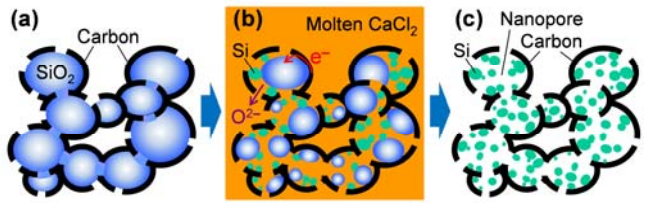


**Fig. 1.** A scheme of electrochemical conversion of $SiO_2$ nanoparticles into Si nanocrystals. (a) $SiO_2$ nanoparticles covered with carbon nanolayer. (b) Electrochemical reduction of the $SiO_2$ nanoparticles into Si nanocrystals in molten $CaCl_2$. (c) Si nanocrystals, together with nanopores, encapsulated with the original carbon layer.

### 2.2 Electrochemical reduction of $SiO_2$ into Si

Electrochemical reduction of $SiO_2$ into Si was carried out by a home-made electrochemical cell utilizing molten $CaCl_2$ (Fig. 2). The system was constructed based on the reports by the Nohira's group.[45,46,47,48,49,53,54] Before the electrochemical experiments, $CaCl_2$ (Wako Pure Chemical Industries, Ltd., 95%) was thoroughly dried up first at 523 K for more than 24 h, and then 773 K for more than 24 h under vacuum. A working electrode was prepared by the following method. A pellet sample was crushed into fine powder and a fraction of the size below 1 mm was collected by sieving. The sample powder (SNP or carbon-coated SNP) was wrapped with a Mo mesh (Nilaco Co., 150 mesh), which was carbon-coated beforehand with a coating apparatus (Vacuum Device Inc., VC-100). Then, the sample-including Mo mesh was rolled and bound with a Mo wire (Nilaco Co., $\phi$ = 0.2 mm, 99.95%), which was connected to a thick Mo wire (Nilaco Co., $\phi$ = 1.0 mm, 99.95%) as shown in Fig. 2. A counter electrode was a graphite rod (Tokai Carbon Co. Ltd., 5×5×50 mm) connected to a thick Mo wire (Nilaco Co., $\phi$ = 1.0 mm, 99.95%). A reference electrode was prepared by immersing an Ag wire (Nilaco Co., $\phi$ = 1.0 mm, 99.99%) into $CaCl_2$ containing 0.5 mol% AgCl (Wako Pure Chemical Industries, Ltd., 99.5%), packed in a mullite tube (Nikkato Co., HB grade, $\phi$ = 6.0 mm). All the potentials for electrochemical experiments were determined by using a quasi-reference electrode prepared by electrodeposition of Ca metal on a Mo wire, in accordance with the Nohira's method.[49] The electrochemical cell was constructed by packing all of the above electrodes in a graphite beaker placed inside a quartz vessel, as shown in Fig. 2. The quartz vessel is embedded in a

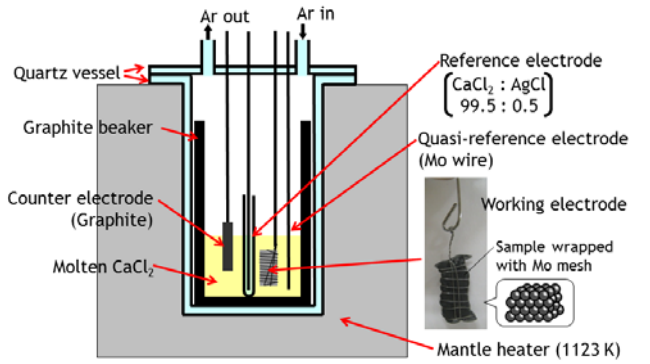


**Fig. 2.** Illustration for the electrochemical cell utilizing molten $CaCl_2$.

mantle heater thereby the cell was heated at 1123 K. All experiments were conducted under Ar atmosphere at 1123 K with an electrochemical workstation HZ-5000 (Hokuto Denko, Co.). Electrochemical behaviors of SNP and carbon-coated SNP were first examined by cyclic voltammetry (CV) at 0.4 mV $s^{-1}$. Then, potentiostatic reduction of the samples was carried out. The sample obtained by the electrochemical reduction of SNP/C(X) (X = 6, 12, or 18) is referred to as SNP/C(X)R. The reduced samples were then washed with HF solution to remove unreduced $SiO_2$. The sample after HF wash is referred to as SNP/C(X)R-HF.

### 2.3 Characterization

The nanostructures of the samples were analyzed with a transmission electron microscope (TEM; JEM-2010, JEOL Ltd.) together with selected area electron diffraction (SAD). The amount of carbon in carbon-coated SNP was estimated from the weight loss when the sample was burnt in a thermogravimetric analyzer (Shimadzu, TGA-51H) at 1173 K for 1 h under air flow. Powder X-ray diffraction (XRD) patterns of the samples were recorded with an XRD-6100 diffractometer (Shimadzu Corporation, Kyoto, Japan) with Cu Kα radiation generated at 30 kV and 20 mA. Nitrogen isotherms of the samples were measured at 77 K with a BEL Japan BELMAX. The specific surface areas ($S_{BET}$) were calculated using the Brunauer–Emmett–Teller (BET) method. The total pore volumes ($V_{total}$) were calculated from the adsorption amount at $P/P_0 = 0.96$. The micropore volumes ($V_{micro}$) were calculated by using the Dubinin-Radushkevich equation. Then, mesopore volumes ($V_{meso}$) were obtained by the following equation: $V_{meso} = V_{total} - V_{micro}$.

Some of electro-reduced samples were subjected to charge/discharge tests as negative electrodes for LIBs, based on a method reported elsewhere.[16,33] Each sample was mixed with conductive additive (Denka Black, Denki Kagaku Kogyo Kabushiki Kaisya) and binder polymers (carboxymethylcellulose (DN-10L, Daicel Fine Chem Ltd.) and styrene butadiene rubber (TRD2001, JSR Corporation)) dissolved in water. The weight ratio of these components was as follows; sample:carbon black:carboxymethylcellulose:styrene butadiene rubber = 67:11:13:9. The resulting slurry was pasted onto a copper foil. After drying at 353 K for 1 h, the foil was cut into a circular shape (16 mm in diameter) to form a working electrode. The working electrode was again dried at 393 K for 6 h under vacuum, and was packed in a three-electrode cell together with a polypropylene separator. A lithium foil was used as a counter and a reference electrode. The electrolyte was 1 M $LiPF_6$ in a mixture of ethylene carbonate and diethyl carbonate (1:1 by volume). CV was performed with a potentiostat/galvanostat (BioLogic, Claix, France; VMP3) between 0.01 and 1.5 V (versus $Li^+/Li$) at a scan rate of 0.1 mV $s^{-1}$. For obtaining Li insertion/extraction capacities, another three-electrode cell was prepared, and it was galvanostatically charged/discharged at a constant current of 200 mA $g^{-1}$ between 0.01 and 1.5 V by using a battery charge/discharge unit (Hokuto Denko Co., Tokyo, Japan; HJ1001). Note that Li insertion and extraction are described as "discharge" and "charge", respectively. All the electrochemical measurements for LIB performance were performed at 298 K.

## 3. Results and discussion

### 3.1 Uniform carbon-coating of $SiO_2$ nanoparticles by P-CVD

Fig. 3a shows a TEM image of SNP. The diameter of most SNP is in the range of 40-50 nm, but smaller particles (ca. 9 nm) are also contained to a small extent.[37] In a typical synthesis process, SNP was molded into a pellet (Fig. 3b), and then the pellet was subjected to P-CVD to carbon-coat the surface of each $SiO_2$ particle (Fig. 3c). As shown in Fig. 3b-c, the morphology of the pelletized SNP is well retained after P-CVD, but the original white color turns completely black by the carbon-coating. The carbon layers formed by P-CVD are extremely thin (less than a few nanometers), and the thickness well correlates with the pulse times, as shown in Fig. 3d-f. In SNP/C(6) (Fig. 3d), the carbon layer is not observed evidently, suggesting that the coating is not perfect. By contrast, SNP/C(12) and SNP/C(18)

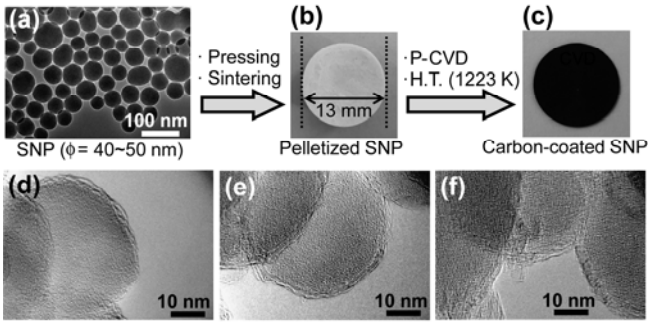


**Fig. 3.** (a) TEM image of SNP; (b,c) Photographs of (b) pelletized SNP and (c) carbon-coated SNP (SNP/C(12)); (d,e,f) TEM images of (d) SNP/C(6), (e) SNP/C(12), and (f) SNP/C(18).

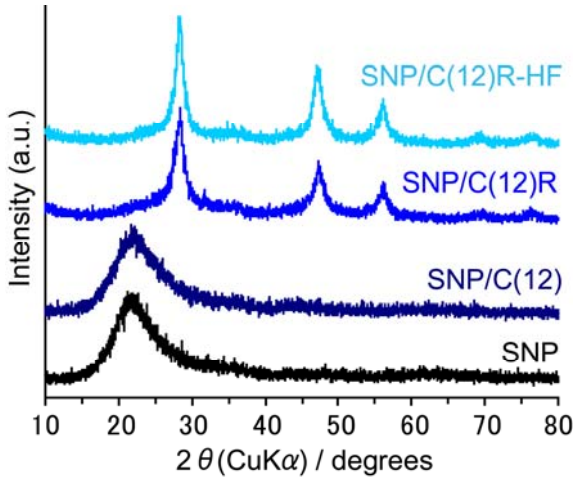


**Fig. 4.** XRD patterns of SNP, SNP/C(12), SNP/C(12)R, and SNP/C(12)R-HF.

samples show homogeneous carbon layers of ca. 1-2 and 2-3 nm in thickness, respectively (Fig. 3e and f).

XRD patterns of SNP/C(12) as well as SNP are shown in Fig. 4, where both samples show only a typical halo peak of amorphous $SiO_2$ at 22°. Fig. 3e clearly indicates the presence of a stacking structure of carbon layers in SNP/C(12), but this sample does not show distinguishable peaks of carbon (002) and (10) at $2\theta = 26$ and 44°, respectively, in Fig. 4. This would be due to the extremely thin thickness as well as relatively low crystallinity of the carbon layer (only ca. 1-2 nm).

### 3.2 Electrochemical reduction of SNP

CV was performed on SNP and SNP/C(18) to investigate their reduction behaviors (Fig. 5). Both samples show four distinguishable cathodic peaks, indicated as (i), (ii), and (iii) in the range of 0.3–1.2 V, and a sharp spike (iv) around 0.2–0.3 V. Considering the CV results reported on bulk $SiO_2$ plates,[45,46,52] (i), (ii), and (iii) can be attributed to the reduction of $SiO_2$ into Si and (iv) corresponds to the formation of Si–Ca alloy. The presence of the three peaks during the $SiO_2$ reduction process indicates that there are different rate steps for the $SiO_2$ reduction into Si in this system. The first peak (i) around 0.9–1.2 V would correspond to a rapid reduction of the samples directly attached to a current collector (Mo mesh). The subsequent two peaks ((ii) and (iii) at around 0.5–0.9 and 0.3–0.5 V, respectively) might be ascribed to the bimodal particle-size distribution of the present SNP, *i.e.*, a minor fraction around 9 nm and a major fraction around 40 nm.[37] Considering such bimodal distribution, the peaks (ii) or (iii) could correspond to the reduction of larger and smaller particles, respectively. It is reasonable to assume that the smaller particles have a slower reduction rate because of the less number of contacting points to other particles, thereby having a larger electric resistance. Though SNP/C(18) has the thickest carbon shell (2–3 nm) in the materials investigated, it shows essentially the same CV pattern as that of SNP. This suggests that the carbon shells actually have defects and/or holes, and the molten $CaCl_2$ can get into the carbon shell to react with the inner $SiO_2$. The CV result in SNP/C(18) suggests that SNP/C(6) and

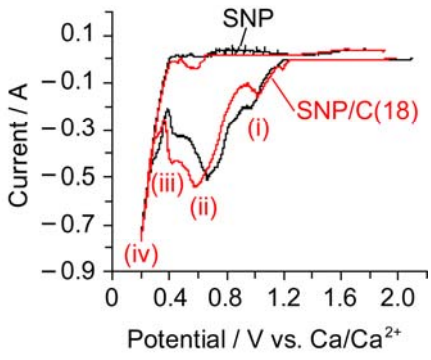


**Fig. 5.** Cyclic voltammograms of SNP and SNP/C(18) in molten $CaCl_2$ electrolyte at 1123 K. Scan rate is 0.4 mV $s^{-1}$. Four peaks of SNP/C(18) are indicated with labels (i)–(iv).

SNP/C(12) could also be electrochemically reduced, because they have thinner carbon shells than SNP/C(18). However, as we will show later, the resulting morphology greatly depends on the thickness of the carbon shells.

Since the reduction of $SiO_2$ into Si occurs below 1.2 V (Fig. 5), we applied a potentiostatic reduction on SNP/C(12) at 1.0 V to prepare the target material shown in Fig. 1c. The reduction was performed by applying successive pulses consisting of reduction steps at 1.0 V and resting steps at an open circuit potential (ca. 2 V) according to the pattern in Fig. 6. The aim of this latter step is to let molten $CaCl_2$ pass through the carbon shell to form the aforementioned three-phase interface, and at the same time, to let the dissolved $O^{2-}$ ions (produced by the reaction (2)) diffuse away from the reaction interface. By assuming that only the reaction (2) takes place, the conversion ratio of $SiO_2$ into Si can be calculated as ca. 60%, based on the total amount of charge passed during the potentiostatic reduction (Fig. 6). As we will show later, the remaining $SiO_2$ can be removed by HF washing, by which additional nanospace is created around Si, and this is advantageous for improving the performance for LIB application. It is actually possible to increase the conversion rate over 90%, simply by extending the

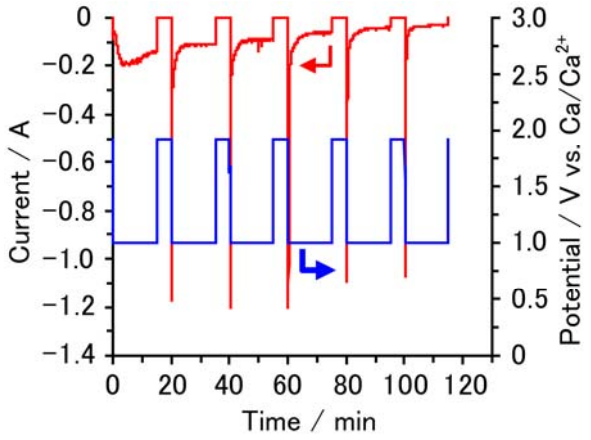


**Fig. 6.** *I-t* curve during potentiostatic reduction of SNP/C(12) at 1.0 V (vs. $Ca/Ca^{2+}$), together with a potential profile.

reduction time. In this case, however, a small amount of SiC tends to be formed as a by-product. Using this conversion ratio together with the carbon fraction in SNP/C(12) determined by the thermogravimetry,[33] the composition of the resulting composite (SNP/C(12)R) can be estimated as Si:$SiO_2$:carbon = 34:49:17 (weight base). The XRD pattern of this electro-reduced sample (Fig. 4) shows three well resolved peaks at $2\theta$ = 28.4°, 47.3°, and 56.1°, corresponding to Si(111), Si(220), and Si(311), respectively, and other peaks from impurities such as SiC or Si–Ca alloy were not evidently observed, indicating the successful reduction of $SiO_2$ into Si without noticeable side reactions. Though the $SiO_2$ peak at $2\theta$ = 22° is greatly weaken after the reduction, a considerable amount of $SiO_2$ residue might still remain in SNP/C(12)R, as was presumed from its composition.

### 3.3 Morphology of the reduced samples

Fig. 7a-d shows TEM images of the electro-reduced samples. Note that *I*-*t* curves for the electro-reduction of SNP/C(6) and SNP/C(18) are shown in the Supporting Information, Fig. S1. In SNP, its original spherical shape (Fig. 3a) was completely lost by the reduction (Fig. 7a), and randomly shaped grains were formed, because of uncontrolled crystal growth of Si. In the reduction product from SNP/C(6) (SNP/C(6)R; Fig. 7b), any trace of the original spherical shape cannot be observed, and a randomly aggregated structure as well as a fibrous structure were observed, suggesting that its carbon shell (Fig. 3d) is so thin and/or defective that the shell was destroyed during the electrochemical reduction. By contrast, the reduced products from SNP/C(12) (SNP/C(12)R; Fig. 7c) and SNP/C(18) (SNP/C(18)R; Fig. 7d) retain spherical morphology derived from their original structures before the reduction. In these samples, it is seen that small grains are encapsulated in hollow carbon shells whose size and shape well agree with those formed on the $SiO_2$ surface (Fig. 3e and f). The highlighted area in Fig. 7d was further analyzed in detail as shown in Fig. 7e (an enlarged TEM image) and 7f (a selected-area electron diffraction (SAD) pattern). Fig. 7e reveals that the spherical carbon shell comprises of stacked carbon layers that correspond to the shells shown in Fig. 7f. Inside the shells, small Si crystals showing its lattice image with a *d*-spacing of Si(111) are observed. The SAD image (Fig. 7f) also proves the presence of Si crystals in the carbon shell. The formation of Si crystals inside the carbon shell means that molten $CaCl_2$ liquid was able to penetrate the carbon shell, and the three-phase interface was formed inside the shell. Not only Si nanocrystals, but also non-crystalline substance is seen in Fig. 7e, as dark regions, and they may be ascribed to unreacted amorphous $SiO_2$. It is found that such remaining $SiO_2$ is much smaller than the original size, and this could be the reason why the remaining $SiO_2$ does not show intense XRD peak as was seen in Fig. 4. Both in SNP/C(12) and SNP/C(18), we have observed a lot of different positions and confirmed that the structures represented in Fig. 7c and d are always seen. Moreover, none of unreacted $SiO_2$ spheres was observed regardless of the size of the carbon shell (Fig. 7c and d). These facts indicates that the reduction occurred throughout the sample both in SNP/C(12) and SNP/C(18).

The XRD measurements revealed the presence of Si in the four samples shown in Fig. 7a-d, but there is a big difference in a half-value width of Si peaks. All the samples derived from carbon-coated SNP (Fig. 7b-d) give broad Si peaks as shown in Fig. 4, whereas the reduction product of uncoated SNP (Fig. 7a) shows very sharp peak as shown in Fig. 8. For the samples shown in Fig. 7a-d, the average crystal sizes of Si are estimated

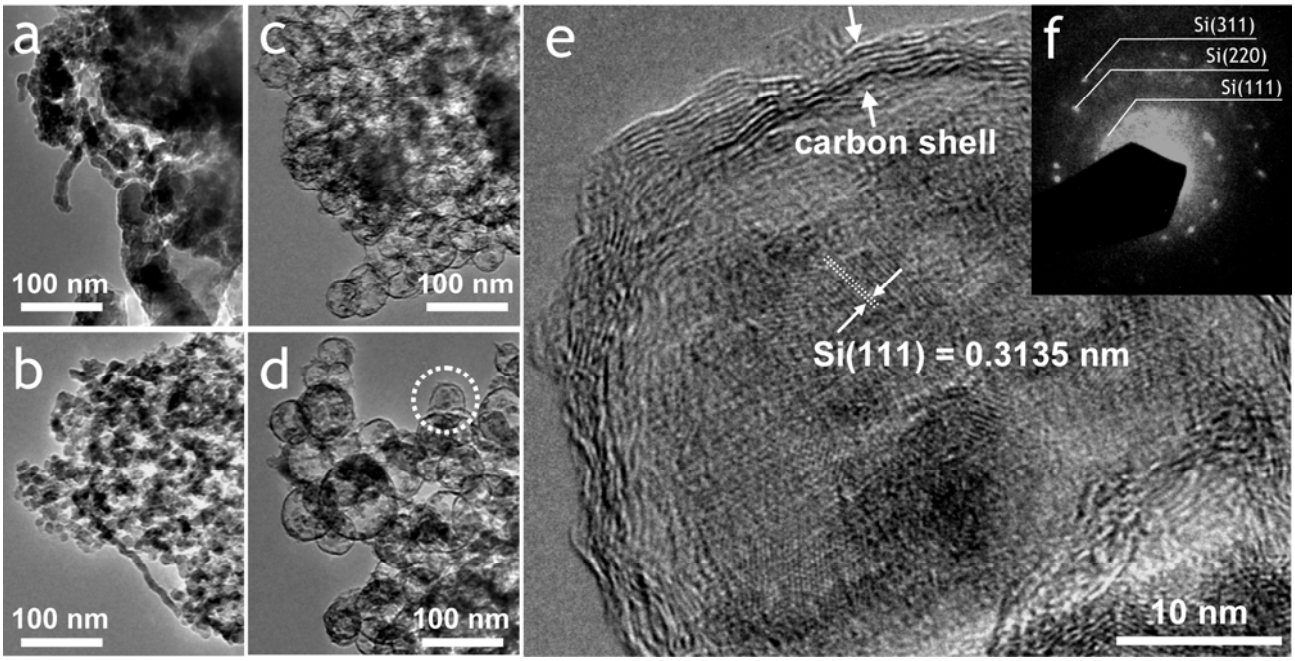


**Fig. 7.** (a-d) TEM images of the samples obtained by the electrochemical reduction of (a) SNP, (b) SNP/C(6), (c) SNP/C(12), and (d) SNP/C(18). The enlarged image and a SAD pattern corresponding to a highlighted area in (d) are shown in (e) and (f), respectively. (a) and (b-d) were reduced by the continuous process and the successive-pulse process, respectively. (a-c) were reduced at 1.0 V, while (d) was reduced at 0.8 V.

to be 81, 18, 17, and 10 nm, respectively, by applying the Scherrer equation to their Si(111) XRD-peaks. As was suggested by Fig. 7a, the reduced product of the uncovered SNP has larger average crystal size than the carbon-coated samples. It is interesting that the randomly aggregated structure in SNP/C(6)R (Fig. 7b) is actually consisting of very small Si nanocrystals (18 nm in average size), although carbon layers were destroyed and their original spherical shape cannot be observed. These results suggest that the thin and defective carbon shells in SNP/C(6) are still effective to restrict the growth of large Si crystals to some extent during the reduction of SNP. In SNP/C(12) and SNP/C(18), the average crystal sizes (17 and 10 nm, respectively) calculated from XRD data accord well to the sizes of the Si nanoparticles observed by TEM (Fig. 7c, d), indicating that Si nanoparticles are single crystals. The difference in their crystal sizes could be related to the different *I-t* curves shown in Fig. 6 and S1b, respectively. In the reduction of SNP/C(18), less intense reduction current flows at an initial stage. This could be ascribed to the thicker carbon shell which restricts more the diffusion of $O^{2-}$ ion. Thus, the reduction of SNP/C(18) proceeded more slowly than SNP/C(12). These results suggest that slower reduction could be effective to reduce the crystal size of Si.

If $SiO_2$ is reduced into Si, its original volume is reduced to 60% after the reduction,[52] so that it is reasonable to leave a cavity around Si as found in Fig. 7c and d. The formation of such cavities can be further analyzed by $N_2$ cryosorption analysis (Fig. 9). SNP/C(12) (the sample before the reduction) is spherical material with a particle size of mainly 40-50 nm (Fig. 3e), showing very small $N_2$ adsorption amount within the whole range of relative pressure ($P/P_0$). However, its reduced product (SNP/C(12)R) shows remarkable $N_2$ uptake and the resulting isotherm can be classified as type IV according to the definition by IUPAC.[55] Thus, the small total pore-volume (0.12 $cm^3\ g^{-1}$) in SNP/C(12) was greatly increased up to 0.92 $cm^3\ g^{-1}$ upon the reduction. The isotherm of SNP/C(12)R is characterized also by a noticeably large hysteresis at a high pressure region, indicating the formation of relatively large nanopores with an ink-bottle-like shape.

We then carried out HF washing of SNP/C(12)R to remove unreacted $SiO_2$. The XRD pattern of the sample after the HF washing (SNP/C(12)R-HF) is shown in Fig. 4. It is found that such HF washing did not affect the XRD pattern of SNP/C(12)R, but the mesopore volume was increased by the HF washing as is found in Fig. 9, *i.e.*, SNP/C(12)R-HF sample

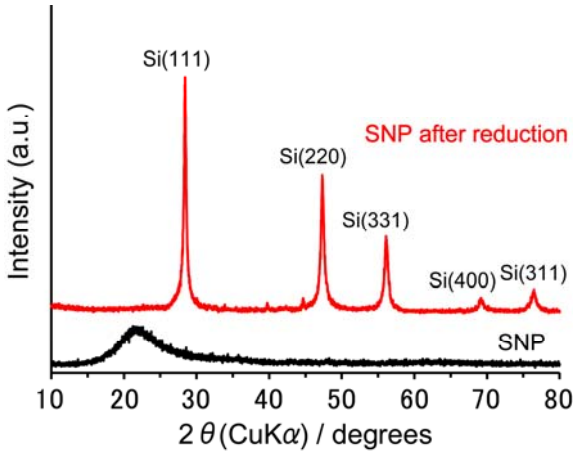


**Fig. 8.** XRD patterns of SNP before and after electoreduction.

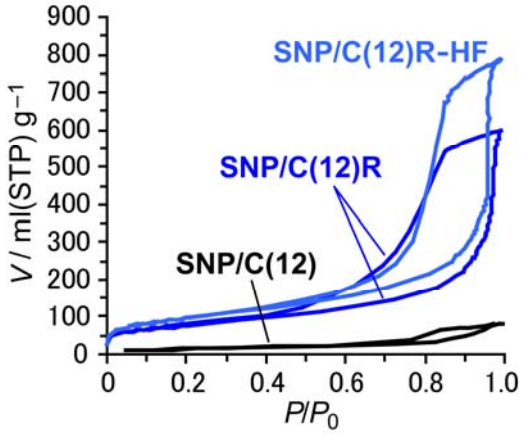


**Fig. 9.** $N_2$ adsorption isotherms (77 K) of SNP/C(12), SNP/C(12)R, and SNP/C(12)R-HF.

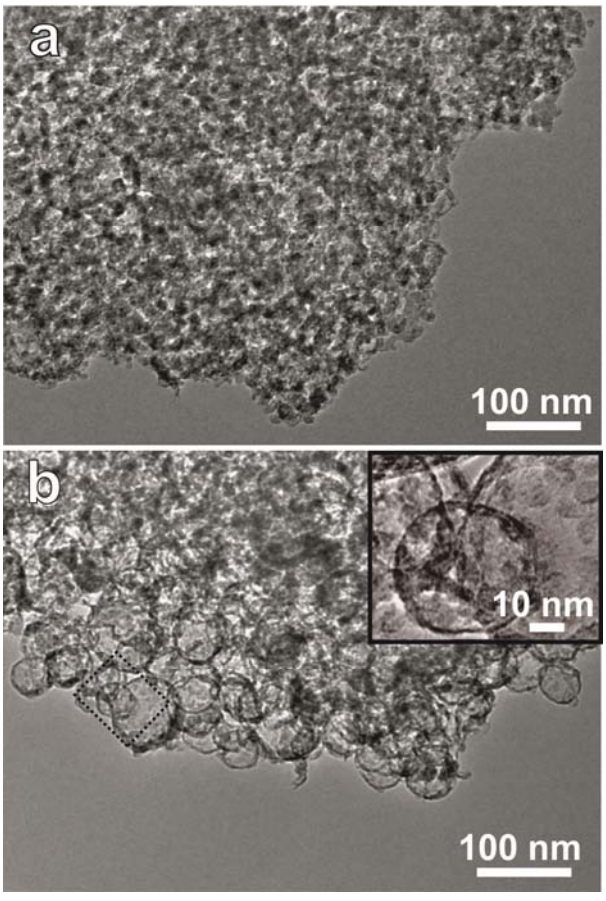


**Fig. 10.** TEM images of (a) SNP/C(6)R-HF and (b) SNP/C(12)R-HF. An enlarged image of the highlighted region by a dotted line in b is shown in an inset.

Table 1. Composition and electrochemical performance of the Si/C nanocomposites.

| Sample | $X_{Si}$ [a] (wt%) | $X_C$ [a] (wt%) | $X_{SiO2}$ [a] (wt%) | $C_{Exp}$ [b] (mAh $g^{-1}$) | $C_{dch1}$ [c] (mAh $g^{-1}$) | $C_{ch1}$ [d] (mAh $g^{-1}$) | $C_{ch20}$ [e] (mAh $g^{-1}$) |
|---|---|---|---|---|---|---|---|
| SNP/C(6)R-HF | 79 | 21 | --- | 2892 | 2533 | 1546 | 633 |
| SNP/C(12)R-HF | 67 | 33 | --- | 2530 | 1948 | 980 | 680 |
| SNP/C(18)R | 39 | 26 | 35 | 1480 | 1263 | 597 | 287 |

[a] Mass content in the Si/C nanocomposites. [b] Expected capacity ($C_{Exp}$) of Si/C nanocomposites calculated by the following equation considering the capacities of carbon ($C_C$) and Si ($C_{Si}$) as 372 and 3572 mAh/g, respectively: $C_{Exp} = (X_{Si} \times C_{Si}) + (X_C \times C_C)$. [c] 1st discharge capacity (Li-insertion process. [d] 1st charge capacity (Li-extraction process). [e] 20th charge capacity. Note that $C_{Exp}$, $C_{dch1}$, $C_{ch1}$, and $C_{ch20}$ are all calculated based on the total composite mass (the weight of Si + carbon).

has a mesopore volume of 1.08 $cm^3$ $g^{-1}$. The increase in the porosity can be ascribed to the removal of unreacted $SiO_2$ in SNP/C(12)R. Also for SNP/C(6)R, HF washing was applied, and TEM images of the samples after HF washing are shown in Fig. 10. Their morphologies are basically similar to those before the HF washing (Fig. 7b and c, respectively). However, dark regions observed in Fig. 7b and c, which are ascribed to unreduced $SiO_2$, are not seen in the samples after the HF washing. The results described above indicate that the target scheme shown in Fig. 1 has been achieved by the electrochemical reduction of SNP/C(12) and the subsequent HF washing.

One of the highlighting advantages of the present approach is the key role of the carbon coating in controlling the growth of Si as well as serving a three-dimensional conductive path. Without the carbon layer, the morphology of Si is absolutely out of control, and random aggregation is formed as a result (Fig. 7a). If the carbon layer is too thin or defective, the layer could be destroyed during the reduction process, and the morphology of the resulting Si is not precisely controlled (Fig. 7b). In order to complete the synthesis scheme shown in Fig. 1, an appropriate thickness is necessary for the carbon layer to act as a physical barrier to restrict the growth of large Si crystal. Under such conditions, Si nanoparticles were successfully formed in the confined nanospace of the carbon shells (Fig. 7c and d). It is thus found that one of the key steps is uniform coating of nano-$SiO_2$ (the precursor of nano-Si) with a thin carbon layer whose thickness is precisely controlled at a level of a few nanometers. The P-CVD method used in this work meets such requirements. Note that P-CVD was performed on a pelletized SNP as shown in Fig. 3b. Though the pelletized SNP is a nanoporous monolith, P-CVD allows uniform carbon-coating throughout such a porous, bulky sample.[16,56] To the contrary, the conventional continuous CVD method does not allow such uniform carbon-coating, rather only the outside surface of the pellet is covered in this case. P-CVD is a simple method and can be applied to any form of $SiO_2$ nanomaterials. Accordingly, the present synthesis pathway (Fig. 1) can be applied to various kinds of $SiO_2$ nanomaterials, such as mesoporous silicas, colloidal crystals, and biosilicas, to fabricate a variety of Si/C nanocomposite materials in which very small Si nanocrystals are embedded in carbon nanoshells having unique morphologies derived from the original $SiO_2$ nanomaterials.

### 3.4 The morphology effect on LIB application

Though Si is considered as one of the most promising negative-electrode materials for next generation LIBs,[11,12,13,14,15,16] Si suffers from a low rate performance due to its low electric conductivity and its low reaction rate with Li.[18,19,23,24] In addition, Si shows a large volume expansion (up to 400%)[33] and contraction during lithiation and delithiation, respectively, which results in pulverization of the particles followed by electric disconnection from the current collector, leading to a rapid capacity fading upon cycling.[6,15] In order to overcome these drawbacks, decreasing the size of Si down to nm-scale, combining such nano-sized Si with conductive carbon, and introducing a buffer space around the nano-Si are recognized to be effective as indicated by the recent advanced researches.[16,31,32,33,34,35,36] SNP/C(6)R-HF and SNP/C(12)R-HF contain similarly small Si nanocrystals, but their morphologies are completely different as shown in Fig. 10. It is thus interesting to examine the morphology effect on LIB application.

The chemical compositions of SNP/C(6)R-HF and SNP/C(12)R-HF are shown in Table 1, together with the expected capacity ($C_{Exp}$) of Si/C composites from their compositions. The charge/discharge curves (1st to 10th cycles) of these samples are shown in Fig. 11a and b, together with illustrations representing their nanostructures. The capacity dependence of these samples on the cycle number is shown in Fig. 11c, and selected capacity values are picked up and listed in Table 1. SNP/C(6)R-HF (Fig. 11a) showed the higher 1st discharge ($C_{dch1}$) and charge ($C_{ch1}$) capacities than SNP/C(12)R-HF, owing to its higher Si content. However, the capacity of this sample rapidly decreases compared to SNP/C(12)R-HF (Fig. 11c). Our previous work revealed that Si expands to ca. 4 times larger than its original volume upon the lithiation and it is thus necessary to arrange buffer space around Si.[33] With a spherical Si nanoparticle, it should be embedded in a spherical space having a diameter of 1.6 times larger than the Si nanoparticle. In Fig. 10a, SNP/C(6)R-HF does not have such large nanospace around nano-Si. By contrast, SNP/C(12)R-HF having the specific core-shell structure (Fig. 10b) showed a better cyclability in Fig. 11c. From its CV pattern, we have also confirmed the reversible

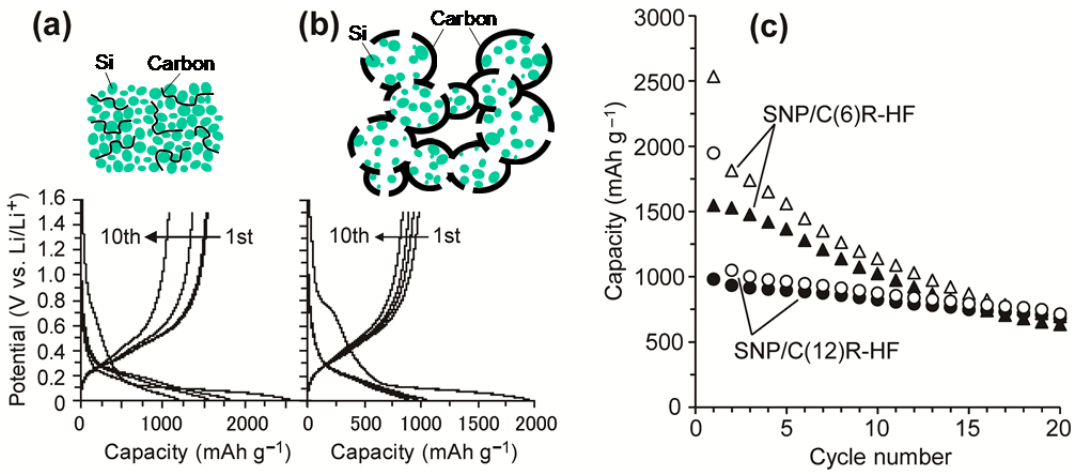


**Fig. 11.** (a,b) Charge/discharge curves (1st, 2nd, 5th, and 10th) of (a) SNP/C(6)R-HF and (b) SNP/C(12)R-HF, together with the illustrations of corresponding nanostructures. Current density is 200 mA $g^{-1}$; (c) Charge/discharge capacities of the samples versus cycle number.

lithiation/delithiation of Si during the cycling (see Fig. S2 in Supporting Information). In SNP/C(12)R-HF, considering its reduction ratio from $SiO_2$ to Si (ca. 60%), the volume of Si is estimated as 1/4 of the volume of its parent $SiO_2$. Since unreduced $SiO_2$ was removed by HF washing, the volume of the buffer nanospace around Si is just 3 times larger than the Si volume in this sample. Thus, the present approach ($SiO_2$ reduction into Si and then HF washing) does realize Si/C nanocomposites having the appropriate buffer size around each Si. Without HF washing, the size of buffer is limited to be simply 1.5 times larger than the size of Si due to the presence of unreduced $SiO_2$. As an example, we have examined the charge/discharge performance of SNP/C(18)R (the sample before HF washing, shown in Fig. 7d and e), and it was found that SNP/C(18)R indeed showed worse performance than SNP/C(12)R-HF (see Fig. S3 in Supporting Information). These results accord to our previous work on the appropriate buffer space, which was prepared by using $SiO_2$ template around nano-Si.[33] In addition, the presence of unreduced $SiO_2$ lowers its $C_{Exp}$, resulting in much lower capacity values than the other samples (Table 1).

Interestingly, the capacity retention of SNP/C(12)R-HF is much better than the model Si/C composite which was prepared in our previous work.[33] The previous model Si/C composite was prepared by the template method, thereby having an ideal sized buffer-nanospace around each of spherical Si nanoparticles (ca. 48 nm in diameter). We believe that the improved performance of SNP/C(12)R-HF is due to the extremely small Si nanoparticles (ca. 17 nm), which must be significantly advantageous for the LIB application. At the same time, Fig. 11 also points out that not only such extremely small Si size but also the surrounding nanostructure, *i.e.*, buffer nanospace and the presence of carbon, governs the performance of Si/C composites.

## 4. Conclusions

We have demonstrated the electrochemical reduction of nanoscaled $SiO_2$ by the aid of a uniform carbon nanolayer. The method gives rise to a new synthesis pathway for nano-Si/C composites, in which extremely small Si single crystals (< 20 nm) are present in hollow carbon nanoshells. $SiO_2$ nanoparticles (below 50 nm in diameter) were first coated with a thin carbon layer (its thickness is a few nanometers) through the pulsed CVD method. Then, the $SiO_2$/C nanocomposites thus prepared were electrochemically reduced in molten $CaCl_2$. By adjusting the thickness of the carbon layer, $SiO_2$ was successfully converted to Si nanocrystals (< 20 nm) inside the spherical carbon shell originally deposited on the $SiO_2$ nanoparticles. Owing to the volume difference of $SiO_2$ and the corresponding Si, nanopores were generated around the Si nanoparticles. Thus, unique Si-C core-shell structure was obtained. The carbon coating layer plays two key roles, *i.e.*, it acts as (i) an electric conductive path to the poorly conductive $SiO_2$ nanoparticles, and (ii) a physical barrier to regulate the Si crystal growth inside the carbon shell. Consequently, unique Si/C nanocomposites have been realized: Si nanocrystals were encapsulated by hollow carbon nanoshells whose morphology is derived from the original $SiO_2$ nanoparticles. We have demonstrated that the unique nanostructure produced by this approach improves the cyclability of Si as a negative electrode for LIBs. The present synthesis method is applicable to a variety of $SiO_2$ nanomaterials, and therefore, it is possible to synthesize a new family of Si/C nanomaterials with carbon shells having morphologies derived from the $SiO_2$ nanomaterials.

## Acknowledgements

We thank Kureha Co. for kindly supplying poly(vinylidene fluoride) binder. We also thank Nissan Chemical Industries Ltd. for kindly supplying Snowtex® solution. This research was partially supported by a NEDO Program, Development of High-Performance Battery System for Next-Generation Vehicles (T.K.); and by the Ministry of Education, Culture,



 

Sports, Science and Technology, Grant-in-Aid for Scientific Research on the Innovative Areas: "Fusion Materials" (Area no. 2206), 23107507 (H.N.).

## Notes and references

[a] Institute of Multidisciplinary Research for Advanced Materials, Tohoku University, 2-1-1, Katahira, Aoba-ku, Sendai, 980-8577, Japan. E-mail: nisihara@tagen.tohoku.ac.jp

[b] Department of Applied Chemistry, Faculty of Engineering, Aichi Institute of Technology, 1247 Yachigusa, Yakusa, Toyota 470-0392, Japan.

[c] School of Chemical Engineering, University of Science and Technology Liaoning, Qianshanzhong Road 185, Anshan 114051, China.

[d] Division of Chemical Process Engineering, Graduate School of Engineering, Hokkaido University, N12W8 Kita-ku, Sapporo 060-8628, Japan.

[e] Chemical Engineering Department, School of Industrial Engineering, University of Malaga, Campus de Teatinos s/n, Malaga, 29071, Spain.

† Electronic Supplementary Information (ESI) available. See DOI: 10.1039/b000000x/

1 Carlson, D. E.; Wronski, C. R., *Appl. Phys. Lett.*, 1976, **28**, 671-673.
2 Tian, B. Z.; Zheng, X. L.; Kempa, T. J.; Fang, Y.; Yu, N. F.; Yu, G. H.; Huang, J. L.; Lieber, C. M., *Nature*, 2007, **449**, 885-889.
3 Jalali, B.; Fathpour, S., *J. Lightw. Tech.*, 2006, **24**, 4600-4615.
4 Soref, R. A., *Proc. IEEE*, 1993, **81**, 1687-1706.
5 Koshida, N.; Koyama, H., *Appl. Phys. Lett.*, 1992, **60**, 347-349.
6 Loncar, M.; Doll, T.; Vuckovic, J.; Scherer, A., *J. Lightw. Tech.*, 2000, **18**, 1402-1411.
7 Ghulinyan, M.; Oton, C. J.; Bonetti, G.; Gaburro, Z.; Pavesi, L., *J. Appl. Phys.*, 2003, **93**, 9724-9729.
8 Tsuda, T.; Nohira, T.; Amezawa, K.; Hachiya, K.; Hagiwara, R.; Raz, O.; Ein-Eli, Y., *Electrochim. Acta*, 2008, **53**, 3650-3655.
9 Holmes, J. D.; Ziegler, K. J.; Doty, R. C.; Pell, L. E.; Johnston, K. P.; Korgel, B. A., *J. Am. Chem. Soc.*, 2001, **123**, 3743-3748.
10 Ding, Z.; Quinn, B. M.; Haram, S. K.; Pell, L. E.; Korgel, B. A.; Bard, A. J., *Science*, 2002, **296**, 1293-1297.
11 Kasavajjula, U.; Wang, C. S.; Appleby, A. J., *J. Power Sources*, 2007, **163**, 1003-1039.
12 Li, H.; Huang, X. J.; Chen, L. Q.; Wu, Z. G.; Liang, Y., *Electrochem. Solid State Lett.*, 1999, **2**, 547-549.
13 Li, H.; Wang, Z. X.; Chen, L. Q.; Huang, X. J., *Adv. Mater.*, 2009, **21**, 4593-4607.
14 Magasinski, A.; Dixon, P.; Hertzberg, B.; Kvit, A.; Ayala, J.; Yushin, G., *Nat. Mater.*, 2010, **9**, 353-358.
15 Tarascon, J. M.; Armand, M., *Nature*, 2001, **414**, 359-367.
16 Iwamura, S.; Nishihara, H.; Kyotani, T., *J. Power Sources*, 2013, **222**, 400-409.
17 Chan, C. K.; Patel, R. N.; O'Connell, M. J.; Korgel, B. A.; Cui, Y., *ACS Nano*, 2010, **4**, 1443-1450.
18 Jung, K. H.; Shih, S.; Kwong, D. L., *J. Electrochem. Soc.*, 1993, **140**, 3046-3064.
19 Cullis, A. G.; Canham, L. T.; Calcott, P. D. J., *J. Appl. Phys.*, 1997, **82**, 909-965.
20 Holmes, J. D., *Science*, 2000, **287**, 1471-1473.
21 Lu, X. M.; Hanrath, T.; Johnston, K. P.; Korgel, B. A., *Nano Lett.*, 2003, **3**, 93-99.
22 Tuan, H. Y.; Lee, D. C.; Korgel, B. A., *Angew. Chem. Int. Ed.*, 2006, **45**, 5184-5187.
23 Morales, A. M.; Lieber, C. M., *Science*, 1998, **279**, 208-211.
24 Wang, Y. Q.; Wang, Y. G.; Cao, L.; Cao, Z. X., *Appl. Phys. Lett.*, 2003, **83**, 3474-3476.
25 Chan, C. K.; Peng, H. L.; Liu, G.; McIlwrath, K.; Zhang, X. F.; Huggins, R. A.; Cui, Y., *Nat. Nanotechnol.*, 2008, **3**, 31-35.
26 Hasegawa, T.; Mukai, S. R.; Shirato, Y.; Tamon, H., *Carbon*, 2004, **42**, 2573-2579.
27 Choi, H. S.; Lee, J. G.; Lee, H. Y.; Kim, S. W.; Park, C. R., *Electrochim. Acta*, 2010, **56**, 790-796.
28 Wang, C. S.; Wu, G. T.; Zhang, X. B.; Qi, Z. F.; Li, W. Z., *J. Electrochem. Soc.*, 1998, **145**, 2751-2758.
29 Ng, S. H.; Wang, J. Z.; Wexler, D.; Konstantinov, K.; Guo, Z. P.; Liu, H. K., *Angew. Chem. Int. Ed.*, 2006, **45**, 6896-6899.
30 Liu, X. H.; Zhang, L. Q.; Zhong, L.; Liu, Y.; Zheng, H.; Wang, J. W.; Cho, J. H.; Dayeh, S. A.; Picraux, S. T.; Sullivan, J. P.; Mao, S. X.; Ye, Z. Z.; Huang, J. Y., *Nano Lett.*, 2011, **11**, 2251-2258.
31 Esmanski, A.; Ozin, G. A., *Adv. Funct. Mater.*, 2009, **19**, 1999-2010.
32 Kim, H.; Cho, J., *Nano Lett.*, 2008, **8**, 3688-3691.
33 Iwamura, S.; Nishihara, H.; Kyotani, T., *J. Phys. Chem. C*, 2012, **116**, 6004-6011.
34 Nakamura, H.; Matsui, Y., *J. Am. Chem. Soc.*, 1995, **117**, 2651-2652.
35 Wang, Z. L.; Gao, R. P. P.; Gole, J. L.; Stout, J. D., *Adv. Mater.*, 2000, **12**, 1938-1940.
36 Wan, Y.; Zhao, D. Y., *Chem. Rev.*, 2007, **107**, 2821-2860.
37 Nishihara, H.; Iwamura, S.; Kyotani, T., *J. Mater. Chem.*, 2008, **18**, 3662-3670.
38 Nishihara, H.; Kwon, T.; Fukura, Y.; Nakayama, W.; Hoshikawa, Y.; Iwamura, S.; Nishiyama, N.; Itoh, T.; Kyotani, T., *Chem. Mater.*, 2011, **23**, 3144-3151.
39 Nishihara, H.; Mukai, S. R.; Yamashita, D.; Tamon, H., *Chem. Mater.*, 2005, **17**, 683-689.
40 Zakhidov, A. A.; Baughman, R. H.; Iqbal, Z.; Cui, C. X.; Khayrullin, I.; Dantas, S. O.; Marti, I.; Ralchenko, V. G., *Science*, 1998, **282**, 897-901.
41 Kroger, N.; Deutzmann, R.; Sumper, M., *Science*, 1999, **286**, 1129-1132.
42 Kroger, N.; Lorenz, S.; Brunner, E.; Sumper, M., *Science*, 2002, **298**, 584-586.
43 Zhou, M.; Shang, L.; Li, B.; Huang, L.; Dong, S., *Electrochem. Commun.*, 2008, **10**, 859-863.
44 Bao, Z. H.; Weatherspoon, M. R.; Shian, S.; Cai, Y.; Graham, P. D.; Allan, S. M.; Ahmad, G.; Dickerson, M. B.; Church, B. C.; Kang, Z. T.; Abernathy, H. W.; Summers, C. J.; Liu, M. L.; Sandhage, K. H., *Nature*, 2007, **446**, 172-175.
45 Nohira, T.; Yasuda, K.; Ito, Y., *Nat. Mater.*, 2003, **2**, 397-401.
46 Yasuda, K.; Nohira, T.; Ogata, Y. H.; Ito, Y., *J. Electrochem. Soc.*, 2005, **152**, D208-D212.
47 Yasuda, K.; Nohira, T.; Hagiwara, R.; Ogata, Y. H., *J. Electrochem. Soc.*, 2007, **154**, E95-E101.
48 Yasuda, K.; Nohira, T.; Amezawa, K.; Ogata, Y. H.; Ito, Y., *J. Electrochem. Soc.*, 2005, **152**, D69-D74.

49 Yasuda, K.; Nohira, T.; Ogata, Y. H.; Ito, Y., *Electrochim. Acta*, 2005, **51**, 561-565.
50 J. Y. Yang, S. G. Lu, S. R. Kan, X. J. Zhang and J. Du, *Chem. Commun.*, 2009, 3273-3275.
51 W. Xiao, X. B. Jin, Y. Deng, D. H. Wang, X. H. Hu and G. Z. Chen, *ChemPhysChem*, 2006, 7, 1750-1758.
52 X. B. Jin, P. Gao, D. H. Wang, X. H. Hu and G. Z. Chen, *Angew. Chem. Int. Ed.*, 2004, 43, 733-736.
53 K. Yasuda, T. Nohira, R. Hagiwara and Y. H. Ogata, *Electrochim. Acta*, 2007, 53, 106-110.
54 K. Yasuda, T. Nohira, K. Takahashi, R. Hagiwara and Y. H. Ogata, *J. Electrochem. Soc.*, 2005, 152, D232-D237.
55 IUPAC, *Pure Appl. Chem.*, 1982, 54, 2201-2218.
56 K. Nueangnoraj, H. Nishihara, K. Imai, H. Itoi, T. Ishii, M. Kiguchi, Y. Sato, M. Terauchi and T. Kyotani, *Carbon*, 2013, 62, 455-464.



 